Hybridized exciton–photon–phonon states in a transition-metal-dichalcogenide van-der-Waals heterostructure microcavity

Donghai Li[1,2], Hangyong Shan[3], Christoph Rupprecht[4], Heiko Knopf[5,6,7], Kenji Watanabe[8], Takashi Taniguchi[9], Ying Qin[10], Sefaattin Tongay[10], Matthias Nuß[1], Sven Schröder[6], Falk Eilenberger[5,6,7], Sven Höfling[4], Christian Schneider[3,4], and Tobias Brixner[1,11*]*

[1] Institut für Physikalische und Theoretische Chemie, Universität Würzburg, Am Hubland, 97074 Würzburg, Germany

[2] University of Science and Technology of China, 230026 Hefei, China

[3] Institute of Physics, University of Oldenburg, D-26129 Oldenburg, Germany

[4] Technische Physik and Wilhelm Conrad Röntgen Research Center for Complex Material Systems, Universität Würzburg, Am Hubland, 97074 Würzburg, Germany

[5] Institute of Applied Physics, Abbe Center of Photonics, Friedrich Schiller University, Albert-Einstein-Straße 15, 07745 Jena, Germany

[6] Fraunhofer-Institute for Applied Optics and Precision Engineering IOF, Albert-Einstein-Straße 7, 07745 Jena

[7] Max Planck School of Photonics, Albert-Einstein-Straße 7, 07745 Jena, Germany

[8] Research Center for Functional Materials, National Institute for Materials Science, 1-1 Namiki, Tsukuba, Ibaraki 305-0044, Japan

[9] International Center for Materials Nanoarchitectonics, National Institute for Materials Science, 1-1 Namiki, Tsukuba, Ibaraki 305-0044, Japan

[10] Materials Science and Engineering, School of Engineering of Matter, Transport, and Energy, Arizona State University, Tempe, AZ 85287, USA

[11] Center for Nanosystems Chemistry (CNC), Universität Würzburg, Theodor-Boveri-Weg, 97074 Würzburg, Germany

[*]E-mails: christian.schneider@uol.de, brixner@uni-wuerzburg.de

Excitons in atomically thin transition-metal dichalcogenides (TMDs) have been established as an attractive platform to explore polaritonic physics, owing to their enormous binding energies and giant oscillator strength. Basic spectral features of exciton polaritons in TMD microcavities, thus far, were conventionally explained via two-coupled-oscillator models. This ignores, however, the impact of phonons on the polariton energy structure. Here we establish and quantify the threefold coupling between excitons, cavity photons, and phonons. For this purpose, we employ energy-momentum-resolved photoluminescence and spatially resolved coherent two-dimensional spectroscopy to investigate the spectral properties of a high-quality-factor microcavity with an embedded WSe_2 van-der-Waals heterostructure at room temperature. Our approach reveals a rich multi-branch structure which thus far has not been captured in previous experiments. Simulation of the data reveals hybridized exciton–photon–phonon states, providing new physical insight into the exciton polariton system based on layered TMDs.

Strong exciton–photon coupling in microcavities gives rise to quasiparticles termed exciton polaritons, emerging as ideal candidates to study phenomena inherent to non-linear bosons by means of optical spectroscopy. Atomically thin monolayers of transition-metal dichalcogenide (TMD) are a very attractive material to investigate the physics of exciton polaritons from cryogenic to room temperature [1–4], owing to their highly interesting excitonic properties, e.g., enormous binding energies and giant oscillator strength [5]. Moreover, the interaction of excitons with phonons governs many important spectral and optoelectronic properties of TMDs [6–9]. Although exciton polaritons have been realized in microcavities with embedded TMD monolayers [1,2] and their van-der-Waals heterostructures [3], the impact of coherent phonon coupling on the energy eigenstates in these systems has not been studied.

It is common practice to employ simple two-coupled-oscillators models to describe the basic spectral features of exciton polaritons emerging in inorganic microcavities [10]. In this model, the strong coupling between a cavity photon E_C (with the excitonic system in the ground state G, thus here labeled as $|E_C;G\rangle$) and an exciton X (with the cavity in its ground state G_C, thus here labeled as $|G_C;X\rangle$) results in two eigenstates, termed upper polariton $|UP\rangle$ and lower polariton $|LP\rangle$, which are both linear superpositions of the cavity photon and the exciton. The role of phonons, however, is usually treated perturbatively, via Boltzmann rate equations, or more involved approaches based on Monte Carlo quantum jumps [11]. In contrast, in organic microcavities, when the vibronic coupling between excitons and phonons competes in strength with the exciton–photon coupling, multiple polariton branches [12,13] and phonon-assisted relaxation [14,15] have been observed experimentally, and were recently directly harnessed to study polaritonic non-linearities down to the single photon level [16]. These observations support a vibronic polariton model which explicitly takes into account not only the degree of freedom of excitons and photons, but also that of phonons [17–19].

The Hamiltonian of a vibronic polariton model can be expressed as [17]

$$H = \begin{pmatrix} E_X & 0 & 0 & g_{00} & g_{01} & g_{02} \\ 0 & E_X + E_V & 0 & g_{10} & g_{11} & g_{12} \\ 0 & 0 & E_X + 2E_V & g_{20} & g_{21} & g_{22} \\ g_{00} & g_{10} & g_{20} & E_C & 0 & 0 \\ g_{01} & g_{11} & g_{21} & 0 & E_C + E_V & 0 \\ g_{02} & g_{12} & g_{22} & 0 & 0 & E_C + 2E_V \end{pmatrix}. \quad (1)$$

Here E_X, E_C, and E_V are the energies of the pure exciton, the cavity photon, and the phonon, respectively. In building the matrix of H, we set the diagonal terms as the energies of three excitonic states, $|G_C;X;v\rangle$, with phonon quantum number v = 0, 1, 2, one pure cavity photon state, $|E_C;G;0\rangle$, and two other phonon-dressed photon states, $|E_C;G;1\rangle$ and $|E_C;G;2\rangle$, which possess energies of $E_C + v\,E_V$ (v = 1, 2). The phonon-dressed photon states consist of one photon plus v phonons of a particular mode. Off-diagonal terms g_{ij} (i, j = 0, 1, 2) are the interaction potentials between the cavity photon and the excitonic states, which can be calculated by [17]

$$g_{ij} = \langle i \,|\, j \rangle \frac{\hbar \Omega_{ij}}{2}, \quad (2)$$

where Ω_{ij} is the Rabi frequency for a particular transition band, and $\langle i \,|\, j \rangle$ represents the vibrational overlap integral (Franck–Condon factor) that depends on the Huang–Rhys factor S. More details of the vibronic polariton Hamiltonian can be found in Supplemental Material [20].

The vibronic polariton model can be understood in a Franck–Condon picture [Fig. 1(a)], wherein the exciton–phonon coupling gives rise to a shift, *d*, along the configurational coordinate of a normal mode of the lattice between the two potential minima, allowing a series of transitions to strongly interact with the cavity photon, and hence, leading to a vibronic polariton progression. In the simplest case, where only the transition between $|G_C;G;0\rangle$ and $|G_C;X;0\rangle$ (i.e., the 0–0 transition for short) strongly interacts with the cavity photon (i.e., g_{ij} are all zero except for g_{00}), the vibronic polariton model approaches the two-coupled-oscillators model, resulting in the polariton dispersion relations shown in Fig. 1(b).

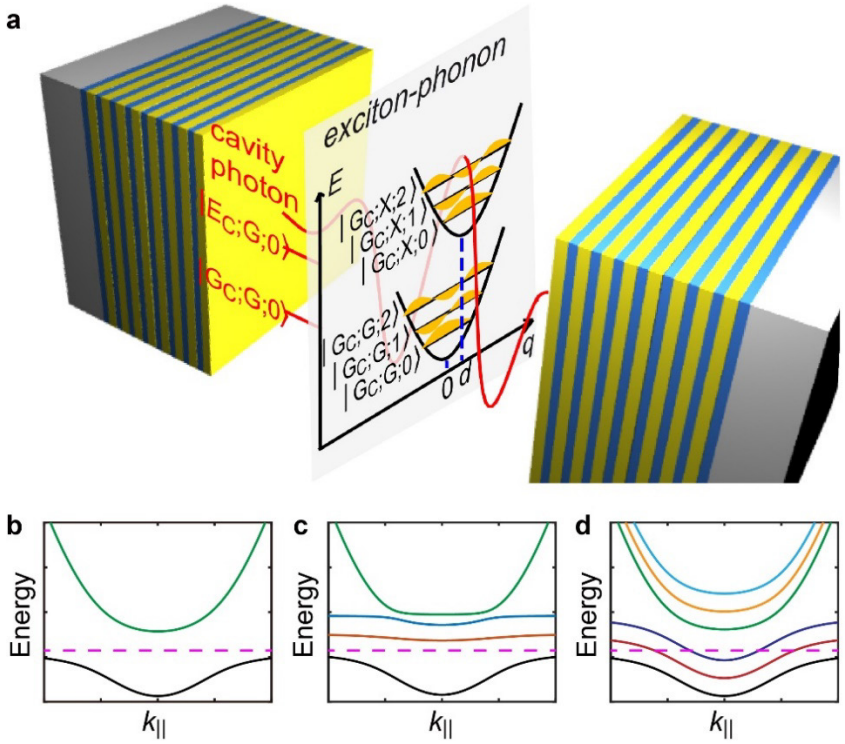

FIG. 1. (a) Schematic plot of the vibronic polariton model. (b) Simulated polariton dispersion curves under two-coupled-oscillator model. (c,d) Simulated polariton dispersion curves using vibronic polariton model under the assumption that the coupling terms with phonon-dressed photon states are deactivated (c) and activated (d). The dashed purple lines indicate the dispersion relation of the pure exciton.

The phonon's degree of freedom can be mixed in through two approaches: (1) large *S*, and/or (2) the inclusion of the phonon-dressed photon states. The first approach is commonly seen in organic microcavities, where the exciton–phonon coupling strength can be as large as that of the exciton–photon coupling, such that g_{01}/g_{10} and g_{02}/g_{20} cannot be ignored anymore. The second approach, on the other hand, is relevant when the excited states of the phonon mode are initially populated, hence the 1–1 and 2–2 transitions can also strongly interact with the cavity photon, and thus Ω_{11} and Ω_{22} are as large as Ω_{00}. We note that for both of the two approaches, it requires a long lifetime of the phonon, such that the vibrational relaxation is slower than the coherent Rabi exchange. Figures 1(b) and 1(c) are the resulting polariton dispersion relations under the Approaches 1 and 2, respectively. Both figure panels show multiple polariton branches. However, for Approach 1 only one branch can be found with an energy below that of pure exciton dispersion (shown as the horizontal dashed line), whereas for Approach 2, because of the inclusion of the phonon-dressed photon states, more than one branch can emerge below the dashed line. We will show that only Approach 2 is consistent with our experimental findings.

Coherent two-dimensional (2D) electronic spectroscopy has emerged as a powerful tool that is sensitive to couplings and dynamic evolution of excitons [28–31] or cavity polaritons [32,33]. We have recently developed fluorescence-detected 2D micro-spectroscopy that provides additional spatial resolution [26], enabling us to acquire 2D spectra from structural domains localized on a μm lateral scale [34]. In the present work, we carry out 2D micro-spectroscopy on a microcavity with an embedded WSe_2 van-der-Waals heterostructure at room temperature. Together with an energy-momentum-resolved photoluminescence (PL) measurement, we observe and quantify vibronic polariton progressions which thus far were not observed in previous reports of TMD-based microcavities.

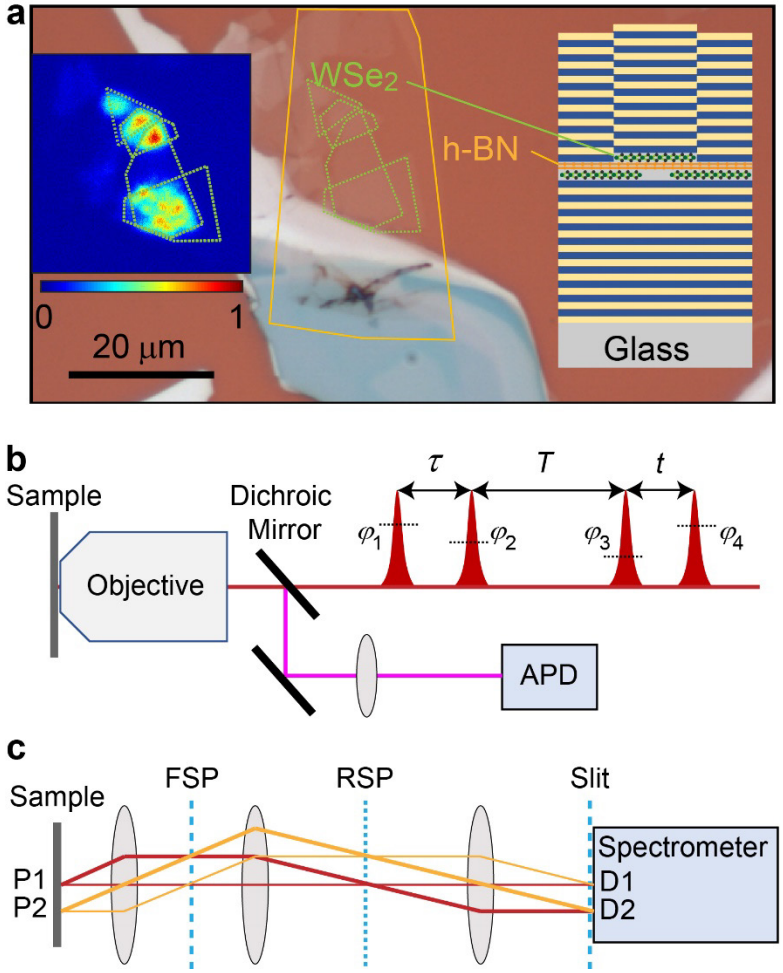

FIG. 2. (a) Microscope image of the WSe_2/h-BN/WSe_2 structure. Insets: Map of PL intensity (left); schematic diagram of the microcavity with embedded WSe_2/h-BN/WSe_2 heterostructure (right). (b) Schematic diagram of 2D micro-spectroscopy. (c) Detection scheme of momentum-resolved PL spectroscopy. Abbreviations: Fourier-space plane (FSP), Real-space plane (RSP), and Avalanche Photodiode (APD).

Figure 2a shows a microscope image of the WSe_2/h-BN/WSe_2 heterostructure as the active material embedded in a microcavity. The four areas indicated with green outlines mark the shapes and locations of four partially overlapping WSe_2 monolayers, hence the WSe_2 heterostructure exhibits single-monolayer and double-monolayer (DML) regions. The WSe_2 monolayers are separated by an h-BN layer (lateral location marked by the orange outline) with a thickness of ~5 nm. The WSe_2/h-BN/WSe_2 van-der-Waals structure is sandwiched between two distributed Bragg reflectors, shown as the right inset of Fig. 2(a) (see Supplemental Material [20] for sample fabrication). The left inset of Fig. 2(a) contains a spatial map of the PL intensity, wherein the DML regions show at maximum ~10 times higher PL than single-

monolayer regions, resulting from both the higher excitation probability and higher PL quantum yield. Thus, we focus on the DML regions throughout this work for obtaining reliable 2D spectral results. For the theoretical model of the DML region, we adopt the standard picture that the cavity photon collectively couples to excitons in both monolayers. Since the two monolayers are approximately degenerate (energetically), the primary effect will be an effective doubling of the oscillator strength, yielding an increase of the Rabi energy by a factor of $\sqrt{2}$.

We carried out 2D micro-spectroscopy and momentum-resolved PL spectroscopy to study the sample. A detailed description of the 2D micro-spectroscopy setup can be found in Supplemental Material [20]. Briefly, four collinear laser pulses generated by a pulse shaper were focused onto the sample by a high-numerical-aperture objective [Fig. 2(b)]. The PL intensity was measured as a function of the three excitation inter-pulse time delays, namely a first coherence time τ, waiting time T, and second coherence time t, as well as the phases of individual pulses φ_{1-4}. A phase-cycling scheme and subsequent Fourier transformation over τ and t allows us to obtain a 2D spectrum for every value of T (find more details of the data acquisition scheme in Supplemental Material [20]). For the momentum-resolved PL measurements, a standard back-Fourier-plane imaging configuration is used [Fig. 2(c)]. Briefly, the first lens on top of the sample and its back-focal plane carries the momentum-dependent information of the sample. A second lens collects the back-focal-plane information of the first lens, and a third lens projects the information into the focal plane (slit) of a spectrometer (find more details in Supplemental Material [20]).

Figure 3(a) shows an energy-momentum-resolved map of the PL intensity for negative $k_{\|}$ measured from one of the DML regions (see Supplemental Material [20] for the full data set). The three most distinct PL features at $k_{\|} = 0$ emerge at ~ 1.605, 1.630, and 1.643 eV, and a ladder-type dispersion can be found at finite $k_{\|}$, as a signature of polaritons in a finite-size trap. A simulation result based on the vibronic polariton model is shown next to it in Fig. 3(b) (find more details of the simulation in Supplemental Material [20]). The multiple polariton dispersion relations emerging with an energy below that of the pure exciton (dotted black) line verify the Approach 2 for the phonon hybridization [Fig. 1(d)].

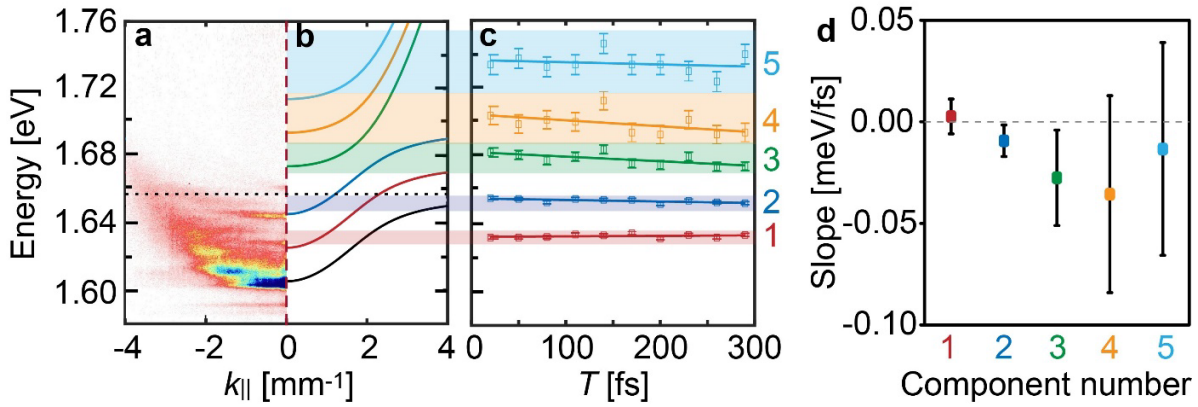

FIG. 3. (a) Energy-momentum-resolved PL map (for negative $k_{\|}$, see Supplemental Material [20] for the full data set). (b) Simulated polariton dispersion relations using vibronic polariton model. The horizontal dotted line indicates the energy of pure excitons. (c) Retrieved energy positions (squares) of five bands as functions of T, and linear fitting results (solid lines). The error bars are evaluated as the standard deviation of the fluctuations calculated from the differences between the measured values (squares) and linear fit results (solid lines) at each T. Colored shaded areas in b and c indicate the total confidence ranges of experimentally determined energy positions from 2D spectroscopy data evaluated over all T, to facilitate comparison with the theoretical dispersion curves. (d) Linear slopes of the five fits from c, with error bars depicting 95% confidence bounds from the fit.

While conventional PL signals probe the population of states, and thus are dominated by photoemission from the lowest excited states only, we can use 2D spectroscopy to obtain full information about the energy structure. i.e., also for the high-energy polariton states that are not visible in PL but that are excited within the broadband laser spectrum. For any quantum system with multiple states in a single-excitation manifold $|E_i\rangle$, the positions of diagonal peaks in a 2D spectrum reveal the energy structure of the system. This can be explained by double-sided Feynman diagrams for the so-called rephasing and non-rephasing contributions [Fig. 4(a)]. The resulting 2D spectra contain two types of pathways resulting in signals at diagonal positions for which excitation and detection frequency are the same, marked in the figure as ground-state bleach (GSB) and stimulated emission (SE) [35]. Each interaction with a laser pulse leads to an optical transition between the ground state $|G\rangle$ and the excited-state manifolds $|E_i\rangle$ in the Feynman diagrams marked either on the right side (change in the ket state) or on the left side (change in the bra state). In all shown cases, the system reaches an excited population state $|E_i\rangle\langle E_i|$ (i = 1, 2, 3, …) after the interactions with the four pulses, and subsequently relaxes to the lowest excited state $|E_0\rangle\langle E_0|$, from which the PL signal is detected. The PL intensity oscillates upon scanning the coherence times, and thus 2D Fourier transformation with respect to τ and t results in a peak in the 2D spectrum whose location is determined by the oscillation frequencies of the coherent states $|G\rangle\langle E_i|$ and $|E_i\rangle\langle G|$ during τ and t, respectively, revealing the energy structure.

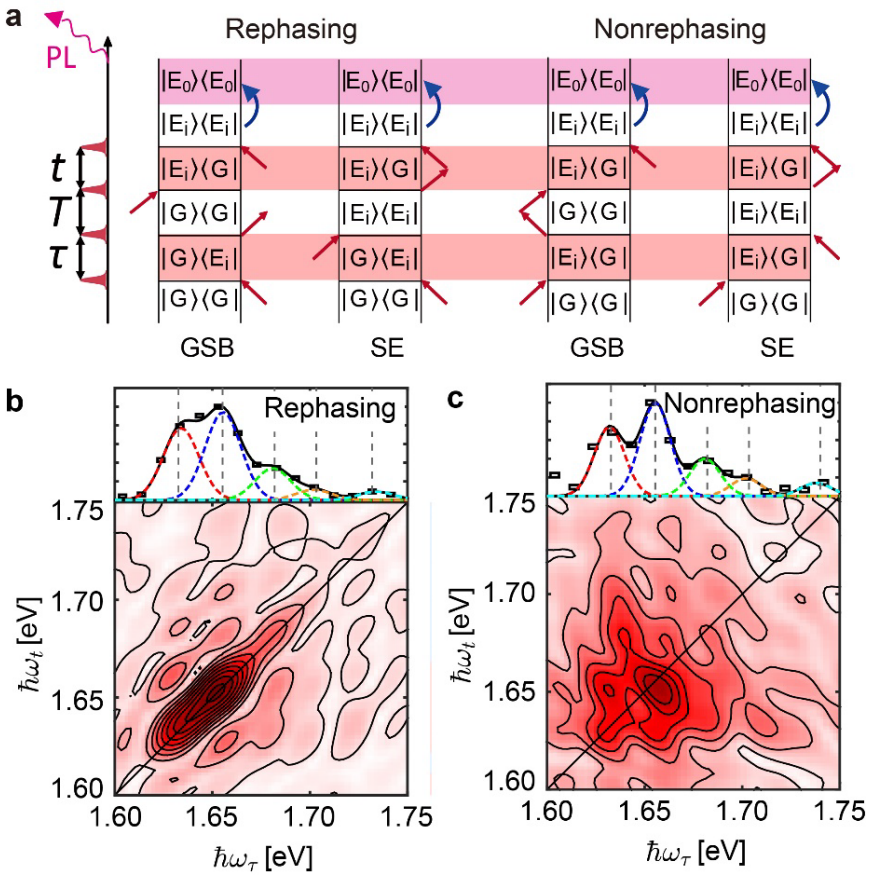

FIG. 4. (a) Feynman pathways corresponding to rephasing and non-rephasing 2D spectra. (b, c) Bottom: Measured rephasing (b) and non-rephasing (c) 2D spectrum (absolute value) at T = 50 fs. Top: Slices through the 2D spectra along the diagonal lines (squares) and the fitting results (black solid curves) using five Gaussian functions (colored dashed curves). Abbreviations: Ground-state bleach (GSB) and stimulated emission (SE).

Figures 4(b,c) show two exemplary 2D spectra at T = 50 fs for rephasing (b) and non-rephasing signals (c). More results for other T can be found in Supplemental Material [20]. The rephasing and the non-rephasing 2D spectra show phase-twisted line shapes: the peaks in the rephasing 2D spectra exhibit elongated line shapes along the diagonal, while in the non-rephasing 2D spectra the peaks are stretched along the anti-diagonal direction. This phase-twisted line shape results from a combination of absorptive and dispersive features [36]. We plot slices along the diagonal lines of the 2D spectra directly on top of the corresponding 2D spectra as black solid lines. Fitting the curves with sums of Gaussians (individual contributions in colored dashed curves) provides the peak positions of five states (vertical gray dashed lines). Fitting results for all diagonal slices of the rephasing and the non-rephasing 2D spectra at different T are given in Supplemental Material [20]. Despite the different line shapes of the rephasing and the non-rephasing 2D signals, the recovered diagonal peak positions agree well with each other, together revealing the same five-peak energy structure. Note that the lowest excited $|E_0\rangle$ state is not initially populated with our particular laser spectrum because of the very low laser intensity at 1.605 eV, and hence the diagonal peak corresponding to $|E_0\rangle$ cannot be observed in 2D spectra. The presence of all higher excited polariton states is a signature of efficient relaxation because in all cases PL is only detected from the lowest state, $|E_0\rangle$ by the employment of a particular optical filter that blocked the PL from higher polariton states.

The reproducibility of the observed energy structure can be proved by measuring 2D spectra at different DML regions on the sample (find more details in Supplemental Materials [20]). In addition, if we plot the line cuts through, e.g., ω_τ = 1.655 eV for the rephasing and the non-rephasing 2D spectra, then the same energy structure can also be found from the positions of off-diagonal peaks (find more details in Supplemental Materials [20]). However, the off-diagonal peaks could be influenced by more Feynman pathways involving two-exciton-manifold energy levels, hence leading to unnecessary complexity. Thus we will focus on the analysis of diagonal peaks throughout the manuscript. The positions of the fourth and fifth peaks show larger uncertainties than the others owing to their low intensities. Therefore, to enhance the relatively weak diagonal peaks located on the high-energy side, we performed an additional 2D measurement at T = 50 fs with the laser spectrum moved to higher excitation energies and total intensity increased to keep the linear PL signal intensity at the same level. As a result, the fourth and fifth diagonal peaks are strongly enhanced such that the peak positions can be more accurately determined, which are 1.702 eV and 1.730 eV, respectively (find more details in Supplemental Material [20]).

Let us now compare the results of the 2D and the energy-momentum-resolved PL spectroscopy. Among the level energies determined from the mean value of the diagonal peak positions within the 2D spectra, the lowest two are located at 1.633 and 1.653 eV. They correspond to the second and the third polariton branches emerging at 1.630 and 1.643 eV observed in the energy-momentum-resolved PL map [Fig. 3(a)]. The diagonal peaks of 2D spectra show energies higher than the PL peaks at $k_{\|}$ = 0, because the 2D spectra measure a momentum-integrated signal, suggesting that the optical excitations are initially distributed over a broader range of $k_{\|}$, followed by relaxation down to the bottom of each branch due to thermalization. As a result, the linear PL signal shows strongest intensity near the zero-momentum position of each branch.

This intra-band relaxation is corroborated by the time-dependent 2D spectra. To reduce the error, the diagonal peak positions at each T were calculated as the mean value of the retrieved peak positions from the rephasing and the non-rephasing 2D spectra and are shown in Fig. 3(c). The positions of the four high-energy components show red-shift behavior with increasing T,

as indicated by the negative slopes of the fitting lines [Fig. 3(d)], reflecting the initial intra-band relaxation within the first 300 fs after the broadband pulsed laser excitation.

An avoided crossing is found in the simulated data between the third and fourth vibronic polariton branches (as counted from the bottom). This is, however, not seen in the momentum-resolved PL measurement, owing to the fact that the decay channels of the high-energy states are so efficient that they are depleted on timescales much faster than their radiative decay. Using 2D spectroscopy, however, we can recover also the high-energy bands located at 1.678, 1.702 and 1.730 eV [Fig. 3(c)]. Owing to the fact that the 2D spectra measure momentum-integrated signals, the diagonal peaks of 2D spectra could be 0–10 meV higher than the bottom energy of the corresponding polariton branch. Considering such a deviation, the experimental peak positions agree well with the simulation results of Fig. 3(b), as indicated by the semi-transparent shaded areas connecting Figs. 3(b) and (c).

By fitting the experimentally determined energy structure with the eigenenergies of the vibronic polariton model, we are able to determine the Hamiltonian (Supplemental Material [20]). For the studied system, the phonon energy was found to be ~ 20 meV, close to that of the E″ phonon mode (21.8 meV) [27]. Due to the Boltzmann distribution, the first and the second excited states of this phonon mode are initially populated at room temperature, such that the 1–1 and 2–2 transitions can strongly interact with the cavity photon, introducing the hybridization of the phonon. Therefore, the observed exciton–photon–phonon hybridization mechanism cannot be simply translated to low temperature, as the initial population of excited phonon states would be strongly reduced, and, at the same time, the formation of trions would further decrease the exciton population. This would explain why in low-temperature experiments, it is often sufficient to work with a two-coupled-oscillators model, whereas the novel observation of hybridized exciton–photon–phonon states emerges only with sufficiently high temperature. Although the A_{1g} phonon mode has been found to couple strongly to excitons in a previous experimental study [7], the extracted phonon energy indicates that the A_{1g} phonon mode is not the source of exciton–photon–phonon hybridization. We speculate that this may be due to a short lifetime of the excited A_{1g} phonon in the excited electronic manifold, which can prevent the vibronic transition to interact strongly with the cavity photon.

To summarize, we studied the nonlinear optical response of a WSe_2/hBN/WSe_2 van-der-Waals heterostructure embedded in a microcavity by employing two-dimensional (2D) micro-spectroscopy and energy-momentum-resolved photoluminescence spectroscopy. The experimental results reveal multiple polariton branches induced by exciton–photon–phonon hybridization that can be modeled by a vibronic polariton Hamiltonian. We thus discover previously unobserved bright states in microcavities with embedded 2D materials. In previous works, phonons have been reported to be crucial in polariton relaxation processes [14,15,37–40]. Hence, we expect that the interaction of TMD microcavities with a phonon bath plays a key role in the energy relaxation down the vibronic polariton progression, which may offer important information for the ongoing attempts of realizing room-temperature Bose–Einstein condensation and polariton lasing in these systems [41].

We thank M. Richard and S. Klembt for fruitful discussions. We acknowledge funding by the European Research Council (ERC) – Projects “MULTISCOPE” with Grant No. 614623 (T.B.) and “Unlimit-2D” with Grant No. 679288 (C.S.). S.T. acknowledges generous support from DOE-SC0020653, NSF-1955889, NSF DMR-1552220, and NSF-1933214. K.W. and T.T. acknowledge support from the Elemental Strategy Initiative conducted by the MEXT, Japan (Grant Number JPMXP0112101001) and JSPS KAKENHI (Grant Numbers 19H05790, 20H00354 and 21H05233). FE and HK are supported by the Federal Ministry of Education and Science of Germany under Grant ID 13XP5053A.

References

[1] X. Liu, T. Galfsky, Z. Sun, F. Xia, E. Lin, Y.-H. Lee, S. Kéna-Cohen, and V. M. Menon, *Strong Light–Matter Coupling in Two-Dimensional Atomic Crystals*, Nat. Photonics **9**, 30 (2015).

[2] N. Lundt, S. Klembt, E. Cherotchenko, S. Betzold, O. Iff, A. V. Nalitov, M. Klaas, C. P. Dietrich, A. V. Kavokin, S. Höfling, and C. Schneider, *Room-Temperature Tamm-Plasmon Exciton-Polaritons with a WSe_2 Monolayer*, Nat. Commun. **7**, 1 (2016).

[3] S. Dufferwiel, S. Schwarz, F. Withers, A. a. P. Trichet, F. Li, M. Sich, O. D. Pozo-Zamudio, C. Clark, A. Nalitov, D. D. Solnyshkov, G. Malpuech, K. S. Novoselov, J. M. Smith, M. S. Skolnick, D. N. Krizhanovskii, and A. I. Tartakovskii, *Exciton–Polaritons in van Der Waals Heterostructures Embedded in Tunable Microcavities*, Nat. Commun. **6**, 1 (2015).

[4] C. Schneider, M. M. Glazov, T. Korn, S. Höfling, and B. Urbaszek, *Two-Dimensional Semiconductors in the Regime of Strong Light-Matter Coupling*, Nat. Commun. **9**, 2695 (2018).

[5] G. Wang, A. Chernikov, M. M. Glazov, T. F. Heinz, X. Marie, T. Amand, and B. Urbaszek, *Colloquium: Excitons in Atomically Thin Transition Metal Dichalcogenides*, Rev. Mod. Phys. **90**, 021001 (2018).

[6] A. M. Jones, H. Yu, J. R. Schaibley, J. Yan, D. G. Mandrus, T. Taniguchi, K. Watanabe, H. Dery, W. Yao, and X. Xu, *Excitonic Luminescence Upconversion in a Two-Dimensional Semiconductor*, Nat. Phys. **12**, 323 (2016).

[7] D. Li, C. Trovatello, S. Dal Conte, M. Nuß, G. Soavi, G. Wang, A. C. Ferrari, G. Cerullo, and T. Brixner, *Exciton–Phonon Coupling Strength in Single-Layer $MoSe_2$ at Room Temperature*, Nat. Commun. **12**, 954 (2021).

[8] G. Wang, M. M. Glazov, C. Robert, T. Amand, X. Marie, and B. Urbaszek, *Double Resonant Raman Scattering and Valley Coherence Generation in Monolayer WSe_2*, Phys. Rev. Lett. **115**, 117401 (2015).

[9] S. Shree, M. Semina, C. Robert, B. Han, T. Amand, A. Balocchi, M. Manca, E. Courtade, X. Marie, T. Taniguchi, K. Watanabe, M. M. Glazov, and B. Urbaszek, *Observation of Exciton-Phonon Coupling in $MoSe_2$ Monolayers*, Phys. Rev. B **98**, 035302 (2018).

[10] A. V. Kavokin, J. J. Baumberg, G. Malpuech, and F. P. Laussy, *Microcavities*, Second Edition (Oxford, New York, 2017).

[11] M. Klaas, H. Flayac, M. Amthor, I. G. Savenko, S. Brodbeck, T. Ala-Nissila, S. Klembt, C. Schneider, and S. Höfling, *Evolution of Temporal Coherence in Confined Exciton-Polariton Condensates*, Phys. Rev. Lett. **120**, 017401 (2018).

[12] R. J. Holmes and S. R. Forrest, *Strong Exciton-Photon Coupling and Exciton Hybridization in a Thermally Evaporated Polycrystalline Film of an Organic Small Molecule*, Phys. Rev. Lett. **93**, 186404 (2004).

[13] L. Fontanesi, L. Mazza, and G. C. La Rocca, *Organic-Based Microcavities with Vibronic Progressions: Linear Spectroscopy*, Phys. Rev. B **80**, 235313 (2009).

[14] D. M. Coles, P. Michetti, C. Clark, W. C. Tsoi, A. M. Adawi, J.-S. Kim, and D. G. Lidzey, *Vibrationally Assisted Polariton-Relaxation Processes in Strongly Coupled Organic-Semiconductor Microcavities*, Adv. Funct. Mater. **21**, 3691 (2011).

[15] T. Virgili, D. Coles, A. M. Adawi, C. Clark, P. Michetti, S. K. Rajendran, D. Brida, D. Polli, G. Cerullo, and D. G. Lidzey, *Ultrafast Polariton Relaxation Dynamics in an Organic Semiconductor Microcavity*, Phys. Rev. B **83**, 245309 (2011).

[16] A. V. Zasedatelev, A. V. Baranikov, D. Sannikov, D. Urbonas, F. Scafirimuto, V. Y. Shishkov, E. S. Andrianov, Y. E. Lozovik, U. Scherf, T. Stöferle, R. F. Mahrt, and P. G. Lagoudakis, *Single-Photon Nonlinearity at Room Temperature*, Nature **597**, 493 (2021).

[17] F. C. Spano, *Optical Microcavities Enhance the Exciton Coherence Length and Eliminate Vibronic Coupling in J-Aggregates*, J. Chem. Phys. **142**, 184707 (2015).

[18] F. Herrera and F. C. Spano, *Theory of Nanoscale Organic Cavities: The Essential Role of Vibration-Photon Dressed States*, ACS Photonics **5**, 65 (2018).
[19] M. A. Zeb, P. G. Kirton, and J. Keeling, *Exact States and Spectra of Vibrationally Dressed Polaritons*, ACS Photonics **5**, 249 (2018).
[20] *See supplemental material at URL for detailed description of vibronic polariton Hamiltonian, sample fabrication, 2D micro-spectroscopy setup, 2D-spectra data acquisition, momentum-resolved PL measurements, 2D spectra for different T, determination of the diagonal peak positions, 2D spectra from different positions, positions of off-diagonal peaks, 2D measurements with higher excitation energies, as well as quantifying the vibronic polariton hamiltonian, which also includes Refs.* [10,17,21–27].
[21] C. Rupprecht, M. Klaas, H. Knopf, H. Knopf, H. Knopf, T. Taniguchi, K. Watanabe, Y. Qin, Y. Qin, S. Tongay, S. Tongay, S. Schröder, F. Eilenberger, F. Eilenberger, F. Eilenberger, S. Höfling, and C. Schneider, *Demonstration of a Polariton Step Potential by Local Variation of Light-Matter Coupling in a van-Der-Waals Heterostructure*, Opt. Express **28**, 18649 (2020).
[22] H. van Amerongen, L. Valkunas, and R. van Grondelle, *Photosynthetic Excitons* (2000).
[23] H. Knopf, N. Lundt, T. Bucher, S. Höfling, S. Tongay, T. Taniguchi, K. Watanabe, I. Staude, U. Schulz, C. Schneider, and F. Eilenberger, *Integration of Atomically Thin Layers of Transition Metal Dichalcogenides into High-Q, Monolithic Bragg-Cavities: An Experimental Platform for the Enhancement of the Optical Interaction in 2D-Materials*, Opt. Mater. Express **9**, 598 (2019).
[24] T. Wu, J. Tang, B. Hajj, and M. Cui, *Phase Resolved Interferometric Spectral Modulation (PRISM) for Ultrafast Pulse Measurement and Compression*, Opt. Express **19**, 12961 (2011).
[25] M. Pawłowska, S. Goetz, C. Dreher, M. Wurdack, E. Krauss, G. Razinskas, P. Geisler, B. Hecht, and T. Brixner, *Shaping and Spatiotemporal Characterization of Sub-10-Fs Pulses Focused by a High-NA Objective*, Opt. Express **22**, 31496 (2014).
[26] S. Goetz, D. Li, V. Kolb, J. Pflaum, and T. Brixner, *Coherent Two-Dimensional Fluorescence Micro-Spectroscopy*, Opt. Express **26**, 3915 (2018).
[27] X. Luo, Y. Zhao, J. Zhang, M. Toh, C. Kloc, Q. Xiong, and S. Y. Quek, *Effects of Lower Symmetry and Dimensionality on Raman Spectra in Two-Dimensional WSe_2*, Phys. Rev. B **88**, 195313 (2013).
[28] T. Brixner, J. Stenger, H. M. Vaswani, M. Cho, R. E. Blankenship, and G. R. Fleming, *Two-Dimensional Spectroscopy of Electronic Couplings in Photosynthesis*, Nature **434**, 625 (2005).
[29] N. S. Ginsberg, Y.-C. Cheng, and G. R. Fleming, *Two-Dimensional Electronic Spectroscopy of Molecular Aggregates*, Acc. Chem. Res. **42**, 1352 (2009).
[30] F. Milota, J. Sperling, A. Nemeth, T. Mančal, and H. F. Kauffmann, *Two-Dimensional Electronic Spectroscopy of Molecular Excitons*, Acc. Chem. Res. **42**, 1364 (2009).
[31] E. Thyrhaug, R. Tempelaar, M. J. P. Alcocer, K. Žídek, D. Bína, J. Knoester, T. L. C. Jansen, and D. Zigmantas, *Identification and Characterization of Diverse Coherences in the Fenna–Matthews–Olson Complex*, Nat. Chem. **10**, 780 (2018).
[32] T. M. Autry, G. Nardin, C. L. Smallwood, K. Silverman, D. Bajoni, A. Lemaître, S. Bouchoule, J. Bloch, and S. Cundiff, *Excitation Ladder of Cavity Polaritons*, Phys. Rev. Lett. **125**, 067403 (2020).
[33] L. Mewes, M. Wang, R. A. Ingle, K. Börjesson, and M. Chergui, *Energy Relaxation Pathways between Light-Matter States Revealed by Coherent Two-Dimensional Spectroscopy*, Commun. Phys. **3**, 1 (2020).
[34] D. Li, E. Titov, M. Roedel, V. Kolb, S. Goetz, R. Mitric, J. Pflaum, and T. Brixner, *Correlating Nanoscale Optical Coherence Length and Microscale Topography in*

Organic Materials by Coherent Two-Dimensional Micro-Spectroscopy, Nano Lett. **20**, 6452 (2020).

[35] P. Malý, J. Lüttig, S. Mueller, M. H. Schreck, C. Lambert, and T. Brixner, *Coherently and Fluorescence-Detected Two-Dimensional Electronic Spectroscopy: Direct Comparison on Squaraine Dimers*, Phys. Chem. Chem. Phys. **22**, 21222 (2020).

[36] M. Khalil, N. Demirdöven, and A. Tokmakoff, *Coherent 2D IR Spectroscopy: Molecular Structure and Dynamics in Solution*, J. Phys. Chem. A **107**, 5258 (2003).

[37] L. Orosz, F. Réveret, F. Médard, P. Disseix, J. Leymarie, M. Mihailovic, D. Solnyshkov, G. Malpuech, J. Zuniga-Pérez, F. Semond, M. Leroux, S. Bouchoule, X. Lafosse, M. Mexis, C. Brimont, and T. Guillet, *LO-Phonon-Assisted Polariton Lasing in a ZnO-Based Microcavity*, Phys. Rev. B **85**, 121201 (2012).

[38] M. Maragkou, A. J. D. Grundy, T. Ostatnický, and P. G. Lagoudakis, *Longitudinal Optical Phonon Assisted Polariton Laser*, Appl. Phys. Lett. **97**, 111110 (2010).

[39] F. Li, L. Orosz, O. Kamoun, S. Bouchoule, C. Brimont, P. Disseix, T. Guillet, X. Lafosse, M. Leroux, J. Leymarie, M. Mexis, M. Mihailovic, G. Patriarche, F. Réveret, D. Solnyshkov, J. Zuniga-Perez, and G. Malpuech, *From Excitonic to Photonic Polariton Condensate in a ZnO-Based Microcavity*, Phys. Rev. Lett. **110**, 196406 (2013).

[40] L. Mazza, L. Fontanesi, and G. C. La Rocca, *Organic-Based Microcavities with Vibronic Progressions: Photoluminescence*, Phys. Rev. B **80**, 235314 (2009).

[41] H. Shan, L. Lackner, B. Han, E. Sedov, C. Rupprecht, H. Knopf, F. Eilenberger, J. Beierlein, N. Kunte, M. Esmann, K. Yumigeta, K. Watanabe, T. Taniguchi, S. Klembt, S. Höfling, A. V. Kavokin, S. Tongay, C. Schneider, and C. Antón-Solanas, *Spatial Coherence of Room-Temperature Monolayer WSe2 Exciton-Polaritons in a Trap*, Nat. Commun. **12**, 6406 (2021).